Proc. 29th Int. Workshop on Vertex Detectors (VERTEX2020)
JPS Conf. Proc. **34**, 010020 (2021)
https://doi.org/10.7566/JPSCP.34.010020

Effect of Thermal Donors Induced in Bulk and Variation in P-stop Dose on the No-gain Region Width Measurements of LGADs

Shudhashil Bharthuar[1,2], Jennifer Ott[1,3], Erik Brücken[1,2], Akiko Gädda[1], Stefanie Kirschenmann[1,2], Maria Golovleva[1,4] and Panja R. Luukka[1,4]
On behalf of CMS collaboration

[1]*Helsinki Institute of Physics, Gustaf Hällströmin katu 2, FI-00014, Finland*
[2]*Department of Physics, University of Helsinki, Gustaf Hällströmin katu 2, FI-00014, Finland*
[3]*Aalto University, Department of Electronics and Nanoengineering, Tietotie 3, Espoo, FI-02150, Finland*
[4]*Lappeenranta-Lahti University of Technology, Yliopistonkatu 34, Lappeenranta, FI-53850, Finland*

E-mail: shudhashil.bharthuar@cern.ch

(Received November 20, 2020)

To cope up with high pile-up rates during Phase-2 operation of the LHC, the CMS experiment will install a precision Minimum Ionising Particle Timing Detector (MTD), between the tracker and calorimeter, which will have a timing resolution of ~30 ps. The endcap part of the MTD, called the Endcap Timing Layer (ETL), will be based on Low-Gain Avalanche Detector (LGAD) Technology.

In this paper, the authors have performed a study on UFSD3.1 LGAD production from Fondazione Bruno Kessler (FBK). The objective of this production was to optimise the interplay between the p-stop dose and the inter-pad terminal strategy. Results show that the nominal no-gain region width value between pads does not affect the breakdown voltage of the sensors at low p-stop doses. A comparative study on the effect of thermal donors induced in the bulk of the sensor was performed by capacitance versus voltage measurements. Further, the property of the sensors were investigated using infra-red (IR) laser, by performing voltage scans and inter-pad profile measurements with gain variation, on changing temperature in Transient Current Technique (TCT). Results show no significant change in the charge collection efficiency and measured no-gain region width values of sensors irrespective of the nature of the bulk.

KEYWORDS: LGAD, TCT, thermal donors, p-stop

1. Introduction

The High-Luminosity LHC (HL-LHC) run will allow an increase in the operational luminosity by a factor of ~5-7, thereby yielding high rates of simultaneous interactions (pile-up) up to values of 140-200 per bunch crossing. To mitigate high pile-up rates, the Compact Muon Solenoid (CMS) experiment will install an additional detector, called MIP Timing Detector (MTD), between the tracker and electromagnetic calorimeter (ECAL) which will allow time of arrival (ToA) measurements that can separate the collisions very close in space as well as in time with a hermetic angular coverage up to a pseudo-rapidity of $|\eta| = 3$. The MTD will provide a notable reconstruction efficiency and a good time resolution of ~30-40 ps, degrading slowly to a magnitude of 50–60 ps due to radiation damage by the end of the HL-LHC operation. This consequently is essential for fulfilling HL-LHC scientific program objectives, which includes the precision measurement of standard model (SM) processes,

especially the characterization of the Higgs boson, as well as searches for Beyond Standard Model (BSM) particles and processes [1].

The MTD will be consisting of a Barrel Timing Layer (BTL) at $|\eta| < 1.5$ and an Endcap Timing Layer (ETL) covering $1.6 < |\eta| < 3$, as shown in Figure 1. The ETL will be based on planar silicon devices with an intrinsic gain of 10-30, called Low-Gain Avalanche Detectors (LGADs). The HL-LHC is expected to deliver an integrated luminosity of 3000 fb^{-1}. The sensors located at the high-η part of the ETL are predicted to receive radiation doses of up to about 450 kGy and a 1 MeV neutron equivalent fluence (neq/cm^2) up to 1.6×10^{15} neq/cm^2 [1].

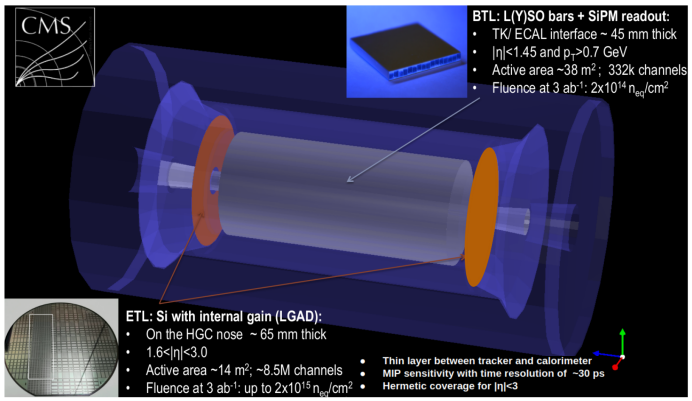

Fig. 1. A schematic layout showing the GEANT simulation geometry of the MTD comprising of the BTL, represented as grey cylinder between the tracker and ECAL, and the ETL, represented as the two orange discs in front of the endcap calorimeter [1].

Type	Nominal Width	Inter-pad design	Strategy
1	16	grid + extra grid	Aggressive
2, 3, 11	21	grid	Medium
4	24	grid	Safe
5	25	grid	Safe
6, 7, 8	28	grid + extra grid	Safe
9	38	2 p-stop	Supersafe
10	49	2 p-stop + bias grid	Supersafe

Fig. 2. A tabulation of the 11 different 'Types' of 2x2 sensors from FBK UFSD3.1 production LGADs from each wafer, defined on the basis of their inter-pad design and nominal no-gain region width.

In this work, the authors have studied the breakdown properties of the non-irradiated LGAD sensors with variation in p-stop dose along with their inter-pad design strategy (as shown in Figure 2), using current versus voltage (I-V) measurements. Further, a comparative study of the sensors depending upon the nature of the bulk, as a result of thermal donors induced in it, has been performed using capacitance versus voltage (C-V) measurements; as well as voltage scans and inter-pad profiles with variation in gain, by changing temperature at a constant voltage, using an IR laser (as the charge deposition by an IR laser mimics that of MIPs) in scanning-TCT.

2. Sensor Specifications

LGADs have intrinsic gain of 10–30 provided by a moderately boron doped p-implant layer, underneath the n$^+$ electrode, which allows impact ionisation giving rise to the multiplication of charge carriers generated within the fully depleted bulk (p$^-$-substrate of the sensor). This p-implant, also known as the gain/multiplication layer, helps to overcome capacitance and other noise sources and achieve a low jitter fast-rising pulse edge that enables precision timing reconstruction for MIPs. Figure 3b shows a cross-sectional view of the active thickness of the LGAD, as mentioned in the MTD Technical Design Report [1]. A good timing performance requires pads with less than a few mm^2 to limit the capacitance of the sensor; meaning that a large number of pixels (pads) with a higher yield are required to cover the 7.9 m^2 area of each of the ETL endcaps. However, the no-gain space between the pads, also called the no-gain region, is responsible for reducing the fill-factor much below 100%. Therefore, optimising the no-gain region width for increasing the fill-factor is crucial in order

to increase the number of two-hit tracks [1]. The no-gain region consists of deep n-doped implants, called junction termination extension (JTE), at the edges surrounded by a p-stop implant to improve the breakdown behaviour of the detector. The nominal no-gain region width, defined as the distance between the gain region of the two adjacent pads of the sensor, is the width based on the mask layout.

The UFSD3.1 production batch LGADs provided by one of the potential vendors, Fondazione Bruno Kessler (FBK), have been studied in this paper. The production consisted of LGADs from six different wafers that differed in their p-stop dose. All the sensors from the six different wafers had the same gain layer dose (with Boron dopant), equivalent to the FBK UFSD2 scale factor of 1.02, as shown in Table 1 of ref. [2]. The main objective behind this production was to optimise the interplay between the no-gain region width and the p-stop dose, such that the breakdown is due to the gain and not due to the geometry of the sensor [3, 4]. In the following paper, sensors from three different wafers; namely W13, W14 and W18 with high, intermediate and low p-stop dose have been measured, respectively. Furthermore, the bulk of the sensors from W18 only did not undergo space charge sign inversion, as explained in detail in Section 3.2. As shown in Figure 3a, each of the sensors have 4 pads (2x2) with a common guard ring around them. Each of the pads has an active area of about 1.3×1.3 mm^2. There are two optical slits, without any metallisation, running across two adjacent pads to subject the laser (Red/Infrared) for Transient Current Technique measurements.

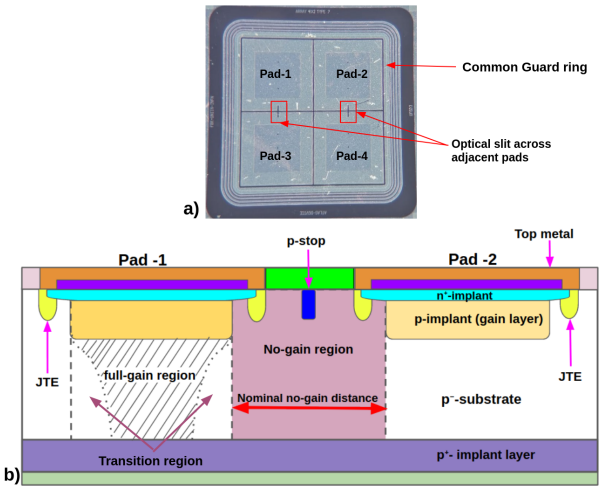

Fig. 3. a) FBK UFSD3.1 production sample with 2x2 pads showing optical slit running across two adjacent pads. b) Cross-sectional view of the active thickness illustrating the gain and no-gain regions across two adjacent pads of an LGAD.

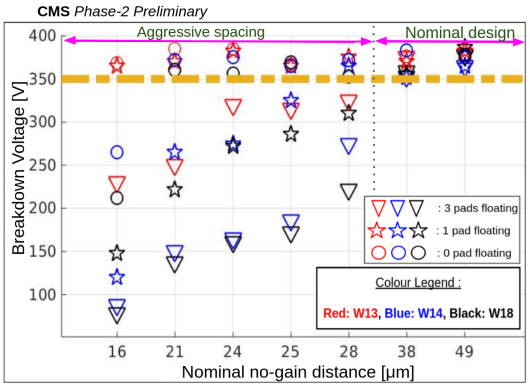

Fig. 4. Breakdown voltage of sensors from three different wafers (W13, W14 and W18) with varying p-stop dose, represented in red, blue, and black color; and different nominal no-gain region widths measured in three different electronic configurations, represented with three separate markers.

3. Electrical Characterisation

3.1 I-V measurements

Figure 4 shows the breakdown voltage values determined from the current versus voltage measurements of sensors with different nominal no-gain region widths from the three different wafers with different p-stop doses and at three different electronic configuration of the pads (i.e. the number of pads that are grounded or are left floating). The idea behind measuring the 2x2 sensors in different electronic configurations is to determine the optimal inter-pad termination design and no-gain region

width value in order to check the robustness of the breakdown voltage even with missing bumps. Sensors that undergo a breakdown due to the gain exhibit a breakdown voltage above 350 V. Therefore, as shown in Figure 4, the threshold is set at 350 V by an orange line. It is important to note that the breakdown due to gain is not a real break of the electric field within the sensor, but is more related to a multiplication of the dark current [5].

One of the consistent results observed in Figure 4 is that for 'Supersafe' sensors with a nominal no-gain region width of 38 µm and 49 µm, the breakdown voltage does not depend on the p-stop dose and the electronic configuration of the pads. In case of sensors with low p-stop doses and aggressive spacing of nominal no-gain region width below 30 µm, the inter-pad strategy does not affect the breakdown voltage unless the remaining three pads are left floating. On increasing p-stop doses, the breakdown of sensors with aggressive, medium and safe nominal no-gain region width not just depends on the inter-pad terminal strategies but is also heavily affected by the number of pads that are grounded/floating. This feature gets predominantly visible for the sensors with no-gain region width below 20 µm. The breakdown voltage decreases for higher p-stop doses because of the high electric field due to the sharp p-n junction generated by the inversion layer, arising from the electrons accumulated due to positive oxide charge, with a highly doped p-stop [6].

3.2 C-V measurements

Bulk capacitance versus bias voltage measurements were performed on sensors from the three different wafers at an AC frequency of 1 kHz and AC signal amplitude of 998.5 mV. Figure 5 shows the inverse square of capacitance versus applied bias voltage plots in order to determine the gain layer depletion voltage and the full depletion voltage of the bulk for the different 'Type' sensors from the three different wafers (W13, W14 and W18) with varying p-stop doses. The gain layer depletion voltage was determined at a bias voltage of 22-23 V, beyond which the inverse square capacitance value exhibits a sharp increase, which corresponds to the depletion of the active bulk region below the gain layer. The full depletion voltage of the bulk, corresponding to values of 25-27 V, was determined as the bias voltage value above which the inverse square capacitance value saturates. Spread in measured capacitance values is observed in the plots for W13 and W14 sensors until the depletion of the gain layer, which affects the extrapolation of the gain layer and bulk depletion voltage by ±2 V.

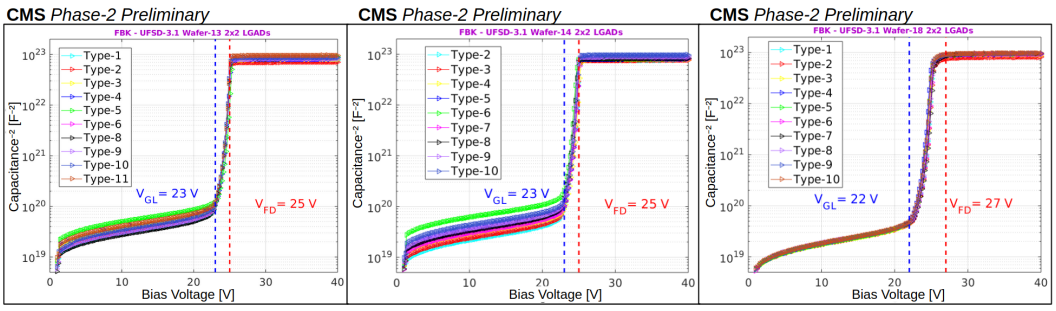

Fig. 5. Inverse square of capacitance vs bias voltage plot for sensors from the three wafers showing the gain-layer depletion voltage and the full depletion voltage of the bulk. The spread in inverse square capacitance values before the gain-layer depletion voltage can be observed in case of W13 and W14 sensors.

The doping profile for the sensors with a constant cross-sectional pad area (A) of 1.3×1.3 mm^2 can be determined from the first derivative of the inverse square capacitance versus voltage (1/C^2-V)

curves by using the following relationship:

$$n(x) = -\frac{C^3}{q\epsilon_{Si}A^2}\left(\frac{dC}{dV}\right)^{-1} = -\frac{2}{q\epsilon_{Si}A^2}\left(\frac{d\frac{1}{C^2}}{dV}\right)^{-1} \quad (1)$$

where the terms $n(x)$, q and ϵ_{Si} are doping density at a depth x of the sensor, fundamental unit of electric charge and permittivity of Silicon, respectively. The above mentioned spread in the capacitance values can be noticed in the shift of the peaks corresponding to the gain layer in the extraction of doping profile plots for W13 sensors shown in Figure 6b. However, no such anomaly in the shift of doping profile peaks corresponding to the gain layer is observed in W18 sensors, as shown in Figure 6a.

The reason behind this anomaly is due to the fact that UFSD3.1 production LGADs have a high resistivity epitaxial substrate, where the bulk is slightly p-doped (almost close to intrinsic), above the Czochralski-Silicon support wafer. Due to high temperature treatments during the processing of the detectors, the oxygen diffuses from the Czochralski substrate into the epitaxial layer. The shallow thermal donors generated via an enhanced concentration of oxygen dimers out-diffusing from the Czochralski substrate cause a space charge sign inversion of the active bulk from p- to n-type [7]. The space charge sign inversion of the bulk due to the induced thermal donors during processing creates a pn-junction not just between the n^+-electrode and gain-layer, but also close to the back-plane due to n-bulk and p^{++}-contact, as shown in Figure 7. Therefore, this gives rise to a double junction. This is unlike the sensors with the p-type bulk where the depletion begins from the top alone. The shift in the doping profile peaks corresponding to the gain layer, observed for W18 sensors, as shown in Figure 6b, is due to the difference in capacitance values. The difference in measured capacitance of the samples is due to the absence of the inter-pad termination design close to the back-plane of the sensor. This gives rise to a difference in the active cross-sectional area, arising majorly due to the region lying outside the sensor. As a result of this anomaly, parasitic capacitance is measured, which is identified by the shift in the doping profiles peaks due to the gain layer. Further, the sign inversion of the bulk results in a lower effective capacitance for sensors with an aggressive no-gain region width compared to more safe designs (as shown in Figure 5), which translates into an apparently more narrow doping profile in Figure 6b.

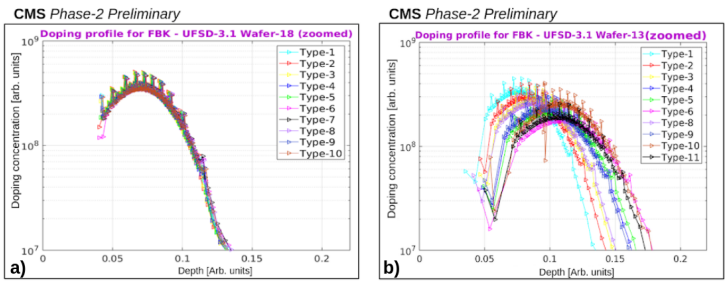

Fig. 6. The doping profile (doping concentration vs. depth) corresponding to the gain layer extracted from C-V measurements for sensors from: a) W18 and b) W13 with different inter-pad termination strategies.

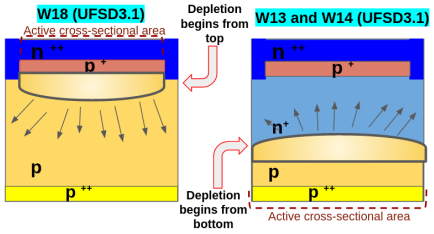

Fig. 7. Thermal donors in the bulk is an anomaly of this production due to unusually high purity silicon and not the nominal design. The figure is a schematic representation of how the depletion begins for the sensors from the different wafers and the effect of space charge sign inversion of the bulk due to thermal donors induced in the bulk.

3.3 Transient Current Technique measurements

In order to study the impact of the space charge sign inversion of the bulk on sensor property, measurements were performed with the Infrared (IR) laser using Particulars based Scanning-Transient current technique (TCT) set-up [8]. A 100 mW, 1064 nm pulsed IR laser with a pulse duration set to 440 ps was used during the measurements. The voltage scans and inter-pad profiles at a constant voltage were studied on varying temperature with IR laser at a low intensity, set to 60% of maximum pulse power with a repetition rate of 1 kHz, equivalent to the charge deposited by 5 MIPs per pulse. The resulting signal pulses are read-out with a Lecroy wavepro (3 GHz analog bandwidth, 20 GS/s) oscilloscope. The oscilloscope is operated in sampling mode, by running an average of 400 measurements for a stored waveform.

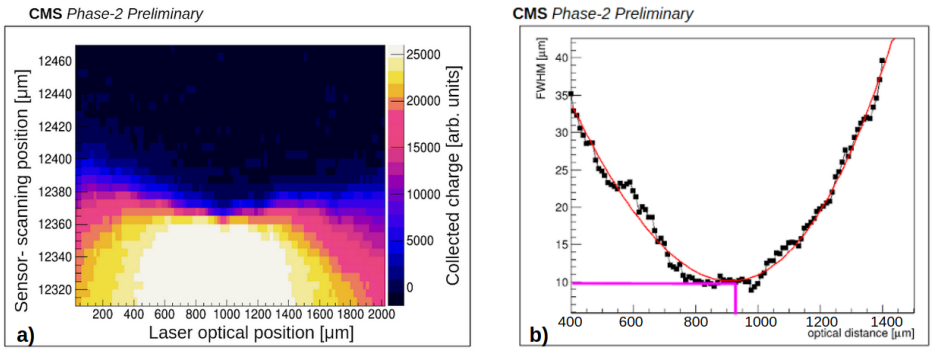

Fig. 8. a) Focus-scan plot showing the focused position of IR laser spot (with respect to the sensor position) where the size of the beam is minimum with maximum flux of photons. b) FWHM vs optical distance of IR laser from sensor showing a size of ∼10 μm laser spot at the focus position.

The knife-edge technique was utilised to locate the optimal focal distance for the laser [9–12]. As shown in Figure 8a, the focal length of the IR laser spot with respect to the sensor surface was determined to be ∼950 μm with Gaussian beam spot of size 10 μm (shown in Figure 8b). All measurements in this study were performed at this focus position of the laser. The inter-pad profile were measured with the IR laser by scanning it across the optical slit running across the two pads at varying temperatures from 25°C to −25°C. The observed inter-pad profile is a convolution of a step function and the Gaussian beam of the IR laser resulting in a S-curve. The measured no-gain region width value is the distance between the 50% amplitude of the convolved function (S-curve) relative to its maximum value, i.e. the distance between the ends of the gain layer between the two adjacent pads [13].

The gain of the sensor depends on the impact ionisation rate, that has an effect on the breakdown properties and the timing resolution of the detector. Impact ionisation is a multiplicative phenomena resulting in the generation of a cascade of electron-hole pairs with high drift velocities due to the strong electric fields within the sensor. The exponential dependence of the impact ionisation rate on temperature makes it crucial to study how the variation of gain with temperature affects the measured no-gain region width, at a constant voltage [14]. Figures 9c and 9d show the inter-pad profiles measured at a constant bias voltage of 285 V from 25°C to −25°C for Type-6 sensors, with nominal no-gain region width of 28 μm, from W13 (with n-type bulk due to the space charge sign inversion resulting from the diffusion of thermal donors) and W18 (with p-type bulk), respectively. The offset between the measured and nominal no-gain region width value is of a magnitude of (10.65 ± 2.20) μm and (6.27 ± 1.10) μm for sensors from W13 and W18, respectively. The preliminary results show that the measured value is ∼3-7 μm higher for sensors from W13. Further, at this constant voltage of

285 V, it is observed that the collected charge under the gain region increases by a factor of ∼2 as the temperature decreases from 25°C to −25°C. Consequently, as the gain increases with decreasing temperature, the increment in the charge collection arising from the edges of the p^+-implant layer (gain layer) and the JTE, with decreasing temperature, impacts the steepness in the slope of the S-curve (measured inter-pad profiles) as one scans across the adjacent pads. As a result of this, the measured no-gain region width value decreases with a decrease in temperature, as the gain increases at the same bias voltage [13]. However, as shown in Table I, the percentage decrease in the measured no-gain region width value is higher for sensors with thermal donors induced in the bulk. This difference in the measured no-gain region width value for sensors from the two wafers is within reasonable systematic uncertainties in the measurement arising due to the fluctuations in laser pulse amplitude and the temperature variations of ± 0.5°C.

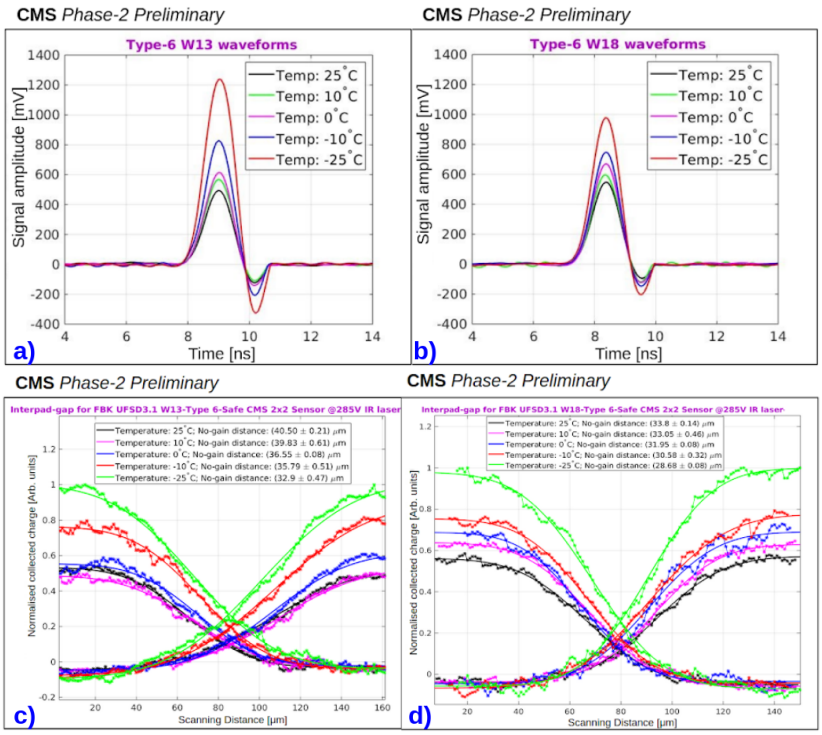

Fig. 9. Comparison in: (i) current signals [a) and b)], and (ii) inter-pad profile measurements [c) and d)] with varying temperature measured at 285 V for Type-6 sensors from W13 and W18, respectively.

The voltage scan plots for Type-6, 9 and 10 sensors from the two wafers (W13 and W18) at varying temperatures is shown in Figure 10. At 25°C, the behaviour in the variation of collected charge with increasing voltage is identical for the sensors irrespective of the nature of the bulk of the sensor. However, in cold measurements, below −10°C, it is observed that the curve gets steeper for W13 sensors as the collected charge increases by a factor of (1.20 ± 0.02), specifically at high bias voltages, with respect to W18 sensors. In addition, the breakdown occurs 15 V earlier than for W18 sensors. This is coherent with the current signal amplitude being ∼ 1.2 times higher for W13 sensors at −25°C, as shown in Figure 9a.

The reason behind the charge collection values being higher for W13 sensors is possibly related to the presence of a 50 Ohm resistor in the HV bias-line of the read-out board, which is responsible for draining more current from the sensors of this wafer as they possess higher surface currents

Table I. Measured no-gain region width values for Type-6, 9 and 10 sensors from sensors from W13 and W18 at varying temperatures. The uncertainties in the measured no-gain region width values are statistical only. The bias voltage is changed for sensors with different nominal no-gain region widths in order to keep the collected charge constant at different values of temperature.

CMS *Phase-2 Preliminary*

Type	W13					W18			
	Nominal no-gain distance value	Measured no-gain distance @			% Decrease in Measured value (from 25ºC to -25ºC)	Measured no-gain distance @			% Decrease in Measured value (from 25ºC to -25ºC)
		25ºC	0ºC	-25ºC		25ºC	0ºC	-25ºC	
Type 6 (285 V)	28	40.50 ± 0.21	36.55 ± 0.08	32.90 ± 0.47	18.77	33.80 ± 0.14	31.95 ± 0.08	28.68 ± 0.08	15.15
Type 9 (300 V)	38	46.38 ± 0.25	40.03 ± 0.06	37.91 ± 0.19	18.26	43.17 ± 0.31	38.39 ±0.67	38.84 ± 0.56	10.03
Type 10 (295 V)	49	60.90 ± 0.09	56.22 ± 0.43	51.90 ± 0.87	13.63	56.41 ± 1.09	55.27 ± 0.90	52.63 ± 0.88	6.70

due to their high p-stop dose. This is viewed as an early breakdown due to limitations in the external read-out electronics, thereby leading to a comparatively higher collected charge as the signal saturates. Therefore, the sensors from W13 experience a higher charge collection value at high bias voltages, close to breakdown, about 15 V earlier than those from W18. Further studies using edge-TCT measurements, where in illumination of the IR laser from the edge of the sensor will allow us to investigate the electric field and collected charge as a function of depth as well as study the impact of temperature [15].

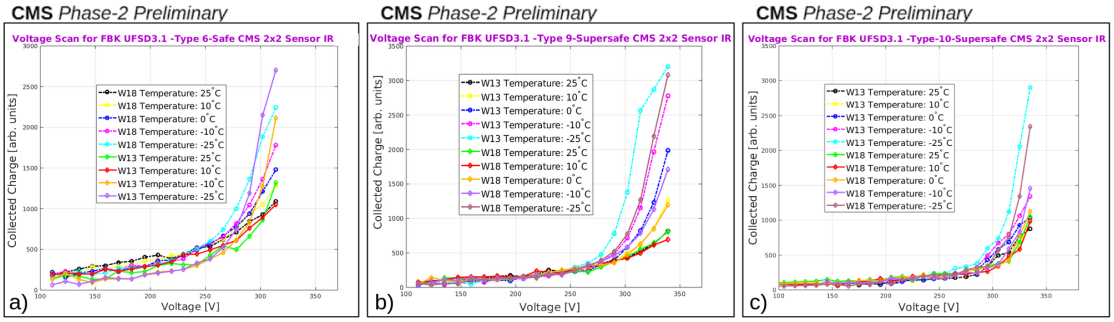

Fig. 10. Voltage scans on temperature variation for Type-6, 9 and 10 sensors from W13 and 18.

4. Summary

The studies performed on the UFSD3.1 LGAD production from FBK are part of the R&D phase for the high-luminosity operation of the CMS detector. By examining the interplay between the variation in the p-stop dose with inter-pad terminal strategy, our studies have shown that the decrease in the p-stop dose improves the breakdown behaviour of the sensors, independent of the no-gain region width between adjacent pads of the sensors.

The spread in the capacitance values in C-V measurements, until the depletion of the gain layer, is observed for sensors with thermal donors induced in the bulk. The thermal donors are induced due to the heating of the detectors during the processing steps, which leads to space charge sign inversion of the bulk. As a consequence of this, a double junction is created. This results in discrepancies in the active cross-sectional area, majorly due to the area lying outside the sensors, contributing to the

measurement of parasitic capacitance values during the depletion of the gain layer. This is identified by the shift in the doping profile peaks corresponding to the gain layer. However, the pad area is not changing, once the sensor is fully depleted. This is proven by the fact that the final value of the capacitance converges to the same value, for all wafers irrespective of the nature of the bulk.

Scanning TCT measurements performed with IR laser, at a constant voltage, show no significant variation in the measured no-gain region width values with increasing gain, the latter being attained by decreasing the temperature, for sensors irrespective of the nature of the bulk. The uncertainties in the measured value lie within the systematic contributions arising from the fluctuations in the laser pulse and temperature variations due to the peltier. Further, there were no significant differences in the charge collection values when measured at room temperature. However, at lower temperatures, the voltage scan curves get steeper for W13 sensors as they drain more current due to the presence of a 50 Ohm resistor in the HV bias line of the read-out board and thereby deliver a slightly higher charge collection value with respect to W18 sensors.

In future, we plan to investigate the timing performance and radiation hardness of LGADs depending on the nature of the bulk. Further, optimisation of the detector processing steps in order to prevent diffusion of thermal donors from the support wafer has been taken into consideration in the future LGADs production runs for the ETL.

5. Acknowledgements

The authors are grateful to Dr. Nicolo Cartiglia, Dr. Valentina Sola and and Dr. Roberta Arcidiacono from Istituto Nazionale di Fisica Nucleare and Universita degli Studi di Torino, Italy for providing us the sensors for our studies. The research is supported by Magnus Ehrnrooth foundation. The authors would like to thank Dr. Eija Tuominen, coordinator of the Detector Laboratory, Helsinki Institute of Physics and the Department of Physics, University of Helsinki, for providing the environment for electrical measurements.

References

[1] CMS collaboration, CERN-LHCC-2019-003, CMS-TDR-020 (2019).
[2] M. Ferrero, R. Arcidiacono, M. Barozzi, et al., Nucl. Instrum. Methods A **919**, 16 (2019).
[3] F. Siviero, presented at The 15th Trento Workshop on Advanced Silicon Radiation Detectors, 2020.
[4] V. Sola, R. Arcidiacono, G. Borghi et al., presented at 35th RD50 Workshop 2019.
[5] V. Sola, R. Arcidiacono, M. Boscardin et al., Nucl. Instrum. Methods A **924**, 360 (2019).
[6] M. Printz, JINST, **10**, C01048 (2015).
[7] G. Lindström, E. Fretwurst, F. Hönniger et al., Nucl. Instrum. Methods A **556**, 451 (2006).
[8] G. Kramberger, Proc. The 23rd International Workshop on Vertex Detectors, Czech Republic, Vol. 227, p. 032 (2015).
[9] J. A. Arnaud, W. M. Hubbard, G. D. Mandeville et al., Appl. Opt. **10**, 2775 (1971).
[10] J. M. Khosrofian and B. A. Garetz, Appl. Opt. **22**, 3406 (1983)
[11] G. Brost, P. D. Horn, and A. Abtahi et al., Appl. Opt. **24**, 38 (1985).
[12] A. H. Firester, M. E. Heller, and P. Sheng, Appl. Opt. **16**, 1971 (1977).
[13] S Bharthuar, J Ott, K Helariutta et al., Nucl. Instrum. Methods A **979**, 164494 (2020).
[14] C. R. Crowell and S. M. Sze, IEEE Transactions on Electron Devices **ED-13**, 677 (1966).
[15] G. Kramberger; V. Cindro; I. Mandić et al., IEEE Trans. Nucl. Sci. **57**, 2294 (2010).